

The lattice thermal conductivity of $\text{Ti}_x\text{Zr}_y\text{Hf}_{1-x-y}\text{NiSn}$ half-Heusler alloys calculated from first principles: Key role of phonon mode nature

Simen N. H. Eliassen,^{1,2} Ankita Katre,³ Georg K. H. Madsen,⁴
 Clas Persson,¹ Ole Martin Løvvik,^{1,5} and Kristian Berland¹

¹*Centre for Materials Science and Nanotechnology,
 Department of Physics, University of Oslo, Norway*

²*Department of Materials Science and Engineering,
 Norwegian University of Science and Technology, Norway*

³*LITEN, CEA-Grenoble, France*

⁴*Institute of Materials Chemistry, TU Wien, Austria*

⁵*SINTEF Materials and Chemistry, Norway*

(Dated: December 9, 2024)

In spite of their relatively high lattice thermal conductivity κ_ℓ , the $X\text{NiSn}$ ($X=\text{Ti}, \text{Zr}$ or Hf) half-Heusler compounds are good thermoelectric materials. Previous studies have shown that κ_ℓ can be reduced by sublattice-alloying on the X -site. To cast light on how the alloy composition affects κ_ℓ , we study this system using the phonon Boltzmann-transport equation within the relaxation time approximation in conjunction with density functional theory. The effect of alloying through mass-disorder scattering is explored using the virtual crystal approximation to screen the entire ternary $\text{Ti}_x\text{Zr}_y\text{Hf}_{1-x-y}\text{NiSn}$ phase diagram. The lowest lattice thermal conductivity is found for the $\text{Ti}_x\text{Hf}_{1-x}\text{NiSn}$ compositions; in particular, there is a shallow minimum centered at $\text{Ti}_{0.5}\text{Hf}_{0.5}\text{NiSn}$ with κ_ℓ taking values between 3.2 and 4.1 W/mK when the Ti content varies between 20 and 80%. Interestingly, the overall behaviour of mass-disorder scattering in this system can only be understood from a combination of the nature of the phonon modes and the magnitude of the mass variance. Mass-disorder scattering is not effective at scattering acoustic phonons of low energy. By using a simple model of grain boundary scattering, we find that nanostructuring these compounds can scatter such phonons effectively and thus further reduce the lattice thermal conductivity; for instance, $\text{Ti}_{0.5}\text{Hf}_{0.5}\text{NiSn}$ with a grain size of $L = 100$ nm experiences a 42% reduction of κ_ℓ compared to that of the single crystal.

I. INTRODUCTION

With their ability to harvest waste heat, thermoelectric materials can help reducing the global energy consumption.^{1,2} A thermoelectric device typically contains pairs of n - and p -type semiconductors, generating an electric current from a difference in temperature T . The energy conversion efficiency of a thermoelectric material is characterized by the dimensionless figure of merit,

$$zT = \frac{\sigma S^2}{\kappa_e + \kappa_\ell} T, \quad (1)$$

where σ is the electrical conductivity, S is the Seebeck coefficient, and κ_e and κ_ℓ are the electronic and lattice thermal conductivity. Thus a high power factor σS^2 is desirable whereas the thermal conductivity κ should be as low as possible. As κ_e is roughly proportional to σ through the Wiedemann-Franz law and often smaller than κ_ℓ in semiconductors, reducing the latter is an important strategy.

Half-Heusler (HH) compounds with the general formula XYZ , crystallize in the $F\bar{4}3m$ spacegroup. The XZ sublattice forms a rock-salt structure of which half the interstitial sites are occupied by Y , so that the YZ sublattice forms a zinc-blende structure. There are many ways to combine three different elements to form HH compounds,³ even when restricted by ther-

modynamic considerations.⁴ This flexibility opens for many potential applications, ranging from spintronics⁵ to optoelectronics.⁶ In particular, the many possibilities allow for the use of inexpensive, earth-abundant and environmentally friendly elements. This is one of the reasons why HH compounds have attracted much attention lately as potential thermoelectric materials.^{3,7-13} The n -type $X\text{NiSn}$ compounds are particularly efficient in the temperature range 400–1000 K and thus hold an important niche where few other competing alternatives exist.^{9,14,15} These compounds often exhibit a high Seebeck coefficient and high electrical conductivity, and thus a high power factor, while their main disadvantage is a relatively high thermal conductivity.¹⁶⁻²⁰

Several studies have demonstrated that isoelectronic sublattice alloying on the X -site of $X\text{NiSn}$ (compounds in the $\text{Ti}_x\text{Zr}_y\text{Hf}_{1-x-y}\text{NiSn}$ family) can drastically reduce the lattice thermal conductivity without considerably reducing electrical conductivity.^{17,18,21-26} There are, moreover, studies showing that introducing barriers like grain boundaries in polycrystalline samples may scatter long-wavelength acoustic phonons, thus reducing κ_ℓ even further,^{19,25,27-32} in particular so for nanostructured bulk samples.³³⁻³⁵

To gain insight into the role of different phonon scattering mechanisms in HH compounds, we calculate in this paper κ_ℓ of $\text{Ti}_x\text{Zr}_y\text{Hf}_{1-x-y}\text{NiSn}$ compounds using density functional theory in conjunction with the Boltzmann

transport equation in the relaxation time approximation. This is combined with anharmonic scattering, calculated in the finite-displacement (frozen phonon) approach,³⁶ mass-disorder scattering arising from alloying of the X sublattice of $X\text{NiSn}$ compounds and the natural abundance of isotopes, as well as boundary scattering. These calculations serve as a theoretical optimization of the alloy composition of $X\text{NiSn}$, probing the potential of combining these effects and guiding efforts to fabricate samples with low thermal conductivity. We explain the trends due to alloying in terms of a competition between the changing nature of the phonon modes and the mass variance. With an optimal alloy combination, we find that the residual heat is carried primarily by low-energetic phonons. Finally, we show how boundary scattering can be utilized to further reduce κ_ℓ by efficiently scattering these phonons.

II. METHOD

A. Lattice thermal conductivity

In the phonon Boltzmann transport equation (BTE) within the relaxation time approximation (RTA),³⁷ the lattice thermal conductivity κ_ℓ for cubic materials is given by

$$\kappa_\ell = \frac{1}{3} \sum_{\mathbf{q}, j} \int \frac{d^3q}{(2\pi)^3} C_{V,j\mathbf{q}} \tau_{j\mathbf{q}} v_{j\mathbf{q}}^2. \quad (2)$$

Here j and \mathbf{q} are the phonon band index and wavevector. The magnitude of the phonon group velocity $v_{j\mathbf{q}}$ is given by the absolute value of the gradient of the phonon dispersion $\omega_{j\mathbf{q}}$. $C_{V,j\mathbf{q}}$ is the heat capacity and $\tau_{j\mathbf{q}}$ the relaxation time. In our calculations, the relaxation time includes contributions from anharmonic three-phonon scattering, $\tau_{j\mathbf{q}}^{\text{anh}}$, mass-disorder scattering $\tau_{j\mathbf{q}}^{\text{md}}$ and grain-boundary scattering $\tau_{j\mathbf{q}}^{\text{bs}}$. For the pure (unmixed) HH compounds $\tau_{j\mathbf{q}}^{\text{md}}$ is made up entirely of isotope scattering. When alloying the X sublattice, $\tau_{j\mathbf{q}}^{\text{md}}$ is generally dominated by mass-disorder on the X site. The total scattering rate (i.e. reciprocal relaxation time) is given by Matthiessen's rule

$$\frac{1}{\tau_{j\mathbf{q}}} = \frac{1}{\tau_{j\mathbf{q}}^{\text{anh}}} + \frac{1}{\tau_{j\mathbf{q}}^{\text{md}}} + \frac{1}{\tau_{j\mathbf{q}}^{\text{bs}}}, \quad (3)$$

where the scattering rate due to mass-disorder is the combined effect of isotope and alloy scattering.

B. Mass-disorder scattering scattering

It is challenging to calculate such scattering explicitly using atomic-scale calculations, but an effective approach is offered by the virtual crystal approximation (VCA).^{38–41} Such substitutions efficiently scatter the

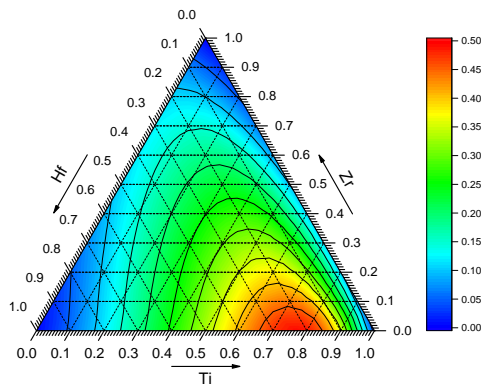


FIG. 1. A color map of the X -site mass variance parameter M_{var} of $\text{Ti}_x\text{Zr}_y\text{Hf}_{1-x-y}\text{NiSn}$.

more energetic phonons, which are carrying a large part of the lattice heat.⁴²

A disordered solid is difficult to model from first principles. For instance, phonon calculations become computationally more demanding when symmetry is broken, such as in alloys, since the number of non-equivalent displacements increases dramatically. The challenges in modeling alloys explicitly motivate using the much simpler virtual crystal approximation (VCA). This assumes that the electronic nature of alloys is similar to that of the respective pure compounds and that its properties can be calculated as an effective compound consisting of mass-averaged atoms.

We use the VCA to represent the disordered sublattice X of the $X\text{NiSn}$ system, with $X = \text{Ti}_x\text{Zr}_y\text{Hf}_{1-x-y}$, as a virtual ("effective") site X_{virtual} . The $X_{\text{virtual}}\text{NiSn}$ system thus retains the symmetry of the pure crystals. The properties of the effective system are calculated by linearly interpolating the masses, that is $m_{\text{virtual}} = x m_{\text{Ti}} + y m_{\text{Zr}} + (1 - x - y) m_{\text{Hf}}$, as well as the second-, and third-order force constants of TiNiSn , ZrNiSn , and HfNiSn . Based on these averages we calculate the phonon dispersion and lattice thermal conductivity of the mixed compositions $\text{Ti}_x\text{Zr}_y\text{Hf}_{1-x-y}\text{NiSn}$.

We find that the trends in the phonon dispersion and lattice thermal conductivity are not very sensitive to whether the forces are interpolated or if the forces of one HH compound is used to represent the virtual crystal (not shown here); the variation of the effective mass with alloy concentration is on the other hand decisive for the trends. This supports that describing alloy scattering in terms of mass-disorder scattering within the VCA is reasonable, and will be used in the following to quantify such scattering.

The scattering rate due to mass-disorder is given by

$$\frac{1}{\tau_{j\mathbf{q}}^{\text{md}}} = \frac{\pi}{6} \omega_{j\mathbf{q}}^2 V \sum_{\mathbf{b}} M_{\text{var}}(\mathbf{b}) |\mathbf{e}(\mathbf{b}|j\mathbf{q})|^2 g_{\mathbf{b}}(\omega_{j\mathbf{q}}). \quad (4)$$

Here $g_{\mathbf{b}}(\omega_{j\mathbf{q}})$ is the partial density of states of atom/site \mathbf{b} in the cell of the virtual crystal. The mass

variance parameter $M_{\text{var}}(\mathbf{b})$ is given by

$$M_{\text{var}}(\mathbf{b}) = \sum_i f_i \left(\frac{\bar{m}(\mathbf{b}) - m(\mathbf{b}; i)}{\bar{m}(\mathbf{b})} \right)^2, \quad (5)$$

where f_i is the relative fraction of species i and $m(\mathbf{b}; i)$ is the mass of atom i at site \mathbf{b} . $\bar{m}(\mathbf{b}) = \sum_i f_i m(\mathbf{b}; i)$ is the average mass. $\mathbf{e}(\mathbf{b}|j\mathbf{q})$ is the phonon amplitude of the atom at site \mathbf{b} corresponding to the phonon mode of band j and wavenumber \mathbf{q} .

The mass variance parameter M_{var} corresponding to the natural distribution of isotopes is at most in the order of 10^{-3} .^{38,39} It is significantly smaller than the M_{var} for the effective crystal on the X sublattice: Figure 1 shows a contour map of M_{var} (eq. 5) for different compositions of $\text{Ti}_x\text{Zr}_y\text{Hf}_{1-x-y}\text{NiSn}$, and it is evident that this is a significantly larger effect with values up to 0.5. The map indi-

$$\frac{1}{\tau_{j\mathbf{q}}^{\text{anh}}} = \frac{36\pi}{\hbar^2} \sum_{j'\mathbf{q}'j''\mathbf{q}''} |\Phi(-j\mathbf{q}, j'\mathbf{q}', j''\mathbf{q}'')|^2 \times \left[(n_{j'\mathbf{q}'} + n_{j''\mathbf{q}''} + 1)\delta(\omega_{j''\mathbf{q}''} - \omega_{j'\mathbf{q}'} - \omega_{j\mathbf{q}}) + 2(n_{j'\mathbf{q}'} - n_{j''\mathbf{q}''})\delta(\omega_{j\mathbf{q}} - \omega_{j'\mathbf{q}'} - \omega_{j''\mathbf{q}''}) \right], \quad (6)$$

where $\Phi(-j\mathbf{q}, j'\mathbf{q}', j''\mathbf{q}'')$ are the third-order force constants³⁷ and $n_{j''\mathbf{q}''}$ is the phonon occupation of the each mode.

D. Boundary scattering

Quantifying grain boundary scattering from an atomic point of view is demanding, given the great variety of boundaries that may exist and the difficulty of treating scattering across even one such boundary explicitly.^{44–46} Nonetheless, an estimate can be obtained with a simple model assuming purely diffusive scattering — every phonon hitting a boundary is completely absorbed and re-emitted during the scattering even.^{43,47} The scattering rate is then given by⁴⁸

$$\frac{1}{\tau_{j\mathbf{q}}^{\text{bs}}} = \frac{v_{j\mathbf{q}}}{L}, \quad (7)$$

where L is the typical grain size, corresponding to the phonon mean free path.

E. Computational details

Electronic structure calculations used to compute second- and third-order force constants, as well as structural properties, are performed with the projector-augmented plane wave method using the Vienna ab initio simulation package VASP.⁴⁹ The exchange-correlation

functional is the generalized gradient approximation (GGA) of Perdew, Burke, and Ernzerhof.⁵⁰ To set up the many atomic configurations required to compute the second- and third-order force constants within the finite-displacement approach, we use the software package PHONO3PY.^{36,51} This package is subsequently used to compute phonon relaxation times and the lattice thermal conductivity. The electronic structure calculations use a $2 \times 2 \times 2$ supercell of the conventional cubic unit cell, representing 96 atoms. The plane-wave cutoff energy is 450 eV and the Brillouin zone is sampled on a $3 \times 3 \times 3$ Monkhorst-Pack \mathbf{k} -point grid using Gaussian smearing and a smearing width of 0.05 eV. The interatomic forces are computed using a displacement length of 0.01 Å. In calculating the phonon relaxation times, we integrate over the Brillouin zone using the tetrahedron method with the phonon modes sampled on a $30 \times 30 \times 30$ \mathbf{q} grid.

Convergence tests indicate that these numerical choices converge the phonon frequencies within ~ 0.03 meV and the κ_ℓ within $\sim 10^{-3}$ W/mK.

III. RESULTS AND DISCUSSION

A. Harmonic properties

The phonon dispersion curves of TiNiSn , ZrNiSn , and HfNiSn are shown in Fig. 2. With three atoms per primitive cell, there are three acoustic and six optical phonon branches. In ionic semiconductors such as

C. Anharmonic scattering

Anharmonic scattering is included at the three-phonon interaction level. Terms beyond the third order are ignored as they are typically less significant at modest temperatures and they are costly to compute. The scattering rate due to anharmonic three-phonon interactions is obtained by using Fermi's golden rule,^{36,43}

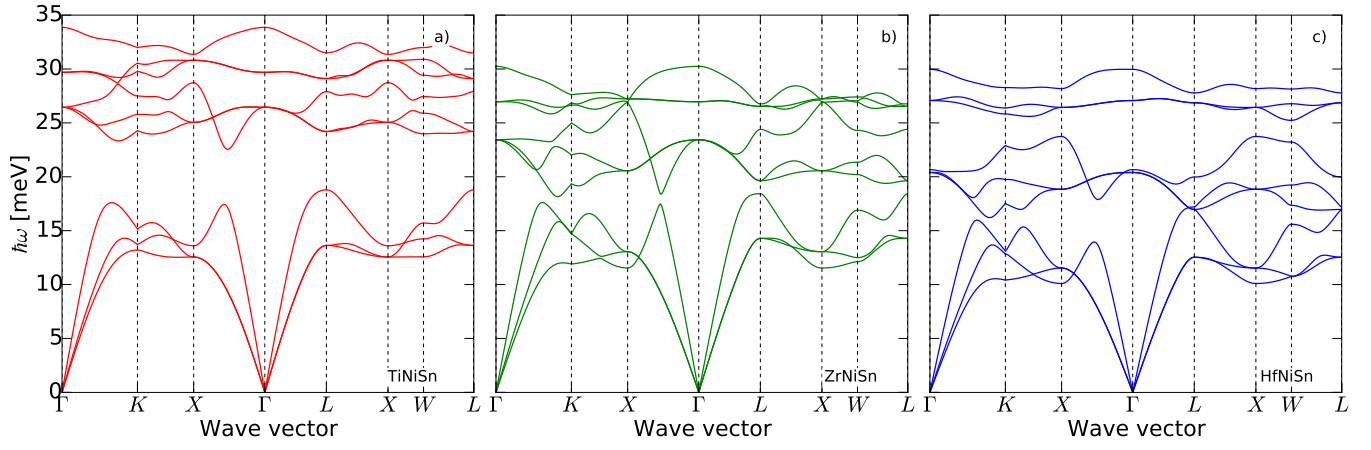


FIG. 2. The phonon dispersion for a) TiNiSn, b) ZrNiSn and c) HfNiSn. The curves for the three compounds are similar, but with a decreasing frequency of the three lower optical phonons bands when going from TiNiSn to HfNiSn.

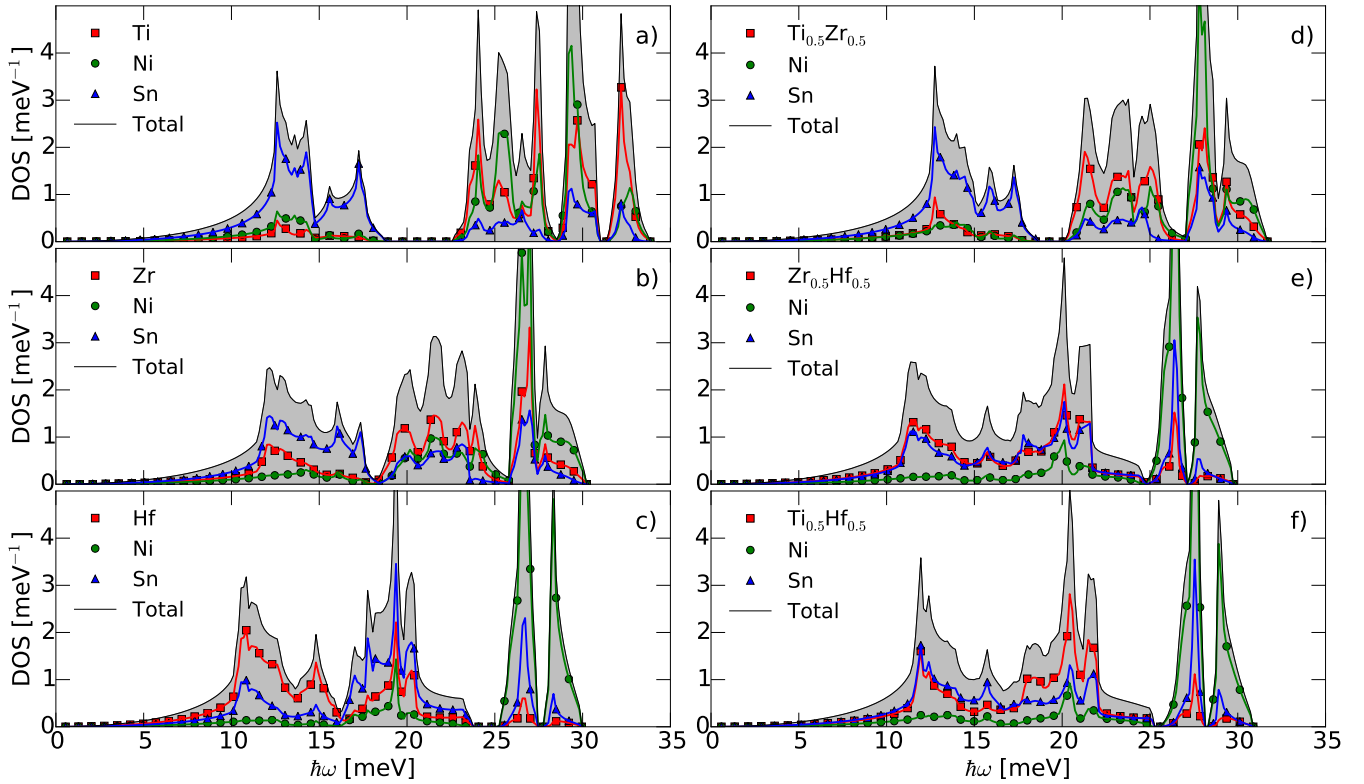


FIG. 3. The full and partial phonon density of states (DOS) for a) TiNiSn, b) ZrNiSn and c) HfNiSn, as well as that of the alloys d) $\text{Ti}_{0.5}\text{Zr}_{0.5}\text{NiSn}$, e) $\text{Ti}_{0.5}\text{Hf}_{0.5}\text{NiSn}$, and f) $\text{Zr}_{0.5}\text{Hf}_{0.5}\text{NiSn}$ obtained in the VCA. The total DOS is shown by the gray, filled area. The partial DOS of the X site (Ti, Zr, Hf, or their mixtures) is given by the red curve, whereas Ni and Sn are shown by the green and blue curves.

the Half Heuslers (HHs), the longitudinal optic (LO) and transverse optical (TO) branches split at the Γ -point. This splitting arises from the induced macroscopic polarization of these modes, an effect that is accounted for by using a non-analytic correction term in the calculations.^{52,53}

The phonon dispersion can be mapped to the phonon density of states (DOS), which is shown in Fig. 3. For TiNiSn (dispersion: Fig. 2a), the acoustic and optical phonon frequencies are separated by a gap throughout the Brillouin zone. This gap decreases with the mass at the X site and is almost closed for ZrNiSn (Fig. 2b),

with the acoustic phonon frequencies decreased by $< 3\%$ and the lower optical phonon frequencies decreased by about 15% compared to those of TiNiSn. For HfNiSn, the three lower optical phonon bands are further decreased by about 13% , closing the gap completely. The upper three optical phonon bands are on the other hand shifted by less than 1% , thus a gap opens between the upper three and the lower three optical bands.

Figure 3 details the partial DOS (PDOS) of the atoms in the unit cell for each of the three pure HHs (a-c) and for the three binary 50-50 mixtures (d-f) as described in the VCA. The phonon modes in the acoustic region are dominated by vibrations of the heaviest atom in the X NiSn compound; in TiNiSn and ZrNiSn this means Sn, while it is Hf in HfNiSn. The mass of the virtual atom X in $Ti_{0.5}Hf_{0.5}NiSn$ and $Zr_{0.5}Hf_{0.5}NiSn$ is 113.2 u and 134.9 u, respectively, which is similar to the Sn mass of 118.7 u. This is reflected in similar PDOS of X and Sn in those compounds, both dominating the DOS over a wide energy span ($\approx 5-22$ meV). The optical phonon modes of highest energy are dominated by vibrations of the lightest atoms; hence Ti and Ni in TiNiSn and Ni in the other compounds. Correspondingly, the lowest energetic optical modes are increasingly dominated by Sn as their frequencies are shifted downwards from TiNiSn to ZrNiSn and HfNiSn. As will be discussed in section III C, the changing nature of the phonon DOS impacts the strength of mass-disorder scattering.

B. Thermal conductivity in bulk X NiSn

TABLE I. The calculated lattice thermal conductivity κ_ℓ computed in this work (boldface) compared with other theoretical calculations and experimental results in the literature.

Compound	κ_ℓ [W/mK]	
	Theory	Experimental
TiNiSn	13.8	9.3^{18}
	15.4^{54}	7.5^{28}
	17.9^3	8^{19}
	16.8^3	
ZrNiSn	15.8	8.8^{18}
	13.4^{54}	10.1^{55}
	19.6^3	6.8^{56}
	17.5^3	5.69^{30} 4.75^{30}
HfNiSn	14.6	6.7^{18}
	15.8^{54}	12^{17}
	19.5^3	6.3^{56} 5.38^{30} 4.8^{30}

Table I compares the bulk calculated lattice thermal conductivities at 300K with earlier published calculations

and experiments. There is a fair spread in the calculated values of κ_ℓ , which can partly be ascribed to different levels of theory; for instance, Andrea et al.⁵⁴ solved the full BTE directly rather than using the relaxation-time approximation.

The calculated κ_ℓ significantly overestimates the experimental data for the unmixed HHs (Table I). Recently, Katre et al. reported that Ni-vacancy-antisite defect pairs have a crucial role of in reducing this difference. By including Ni-vacancy-antisite scattering, obtained from density-functional theory calculations, they predicted κ_ℓ s in good agreement with experimental numbers for realistic defect concentrations. For instance for ZrNiSn, with a defect-pair concentration of 2.9% , κ_ℓ is reduced to 7.4 W/m/K, and for 4% , it is reduced to 5.8 W/m/K. Real samples are likely to contain significant amounts of such defects,⁵⁷⁻⁵⁹ or the related Ni interstitial defects, which may reduce the κ_ℓ considerably by scattering phonon modes of higher energy.⁶⁰ In particular, a high solubility of Ni interstitials has been reported.⁶¹⁻⁶⁵ The overestimation of κ_ℓ by theory of the unmixed X NiSn HHs can thus, at least partially, be explained by the presence of localized defects.

Another potential mechanism reducing the lattice thermal conductivity is grain boundary scattering. In section III D we discuss how this scattering may significantly lower κ_ℓ when the grain size is reduced to the nanoscale. Metallic inclusions, which Katayama et al.⁶⁶ reported present in TiNiSn, could also reduce the lattice thermal conductivity. Another possible source of discrepancy is the lack of fourth-order phonon-phonon scattering in the computations. Such scattering can lower thermal conductivity noticeably, especially at high temperatures.⁶⁷ But this does not change the fact that localized Ni-related defects appear to be the main mechanism for reducing κ_ℓ of the unmixed HH compounds.⁶⁰

C. The effect of alloying

Figure 4 shows κ_ℓ as a function of composition for the two binary HH alloy systems $Ti_xHf_{1-x}NiSn$ and $Zr_xHf_{1-x}NiSn$, comparing our theoretical results with experiment. The modeling exhibits a characteristic U -shape of the thermal conductivity versus composition; that is, κ_ℓ drops drastically when moving from alloy composition $x = 0$ to 0.1 , whereas the change is significantly smaller in the range $x = 0.1 - 0.9$. This arises because a relatively low substitution is sufficient to scatter most of the relevant phonons.⁴¹ However, the drop is far less drastic for the experimental samples and unlike for the unmixed HHs, the computed κ_ℓ is in quite good agreement with experiment for both temperatures in Fig. 4 (300 and 600 K).

To understand why the agreement between theory and experiment is so much better for the mixed compounds, first bear in mind that the main additional scattering mechanisms when alloying on the X sublattice is mass-

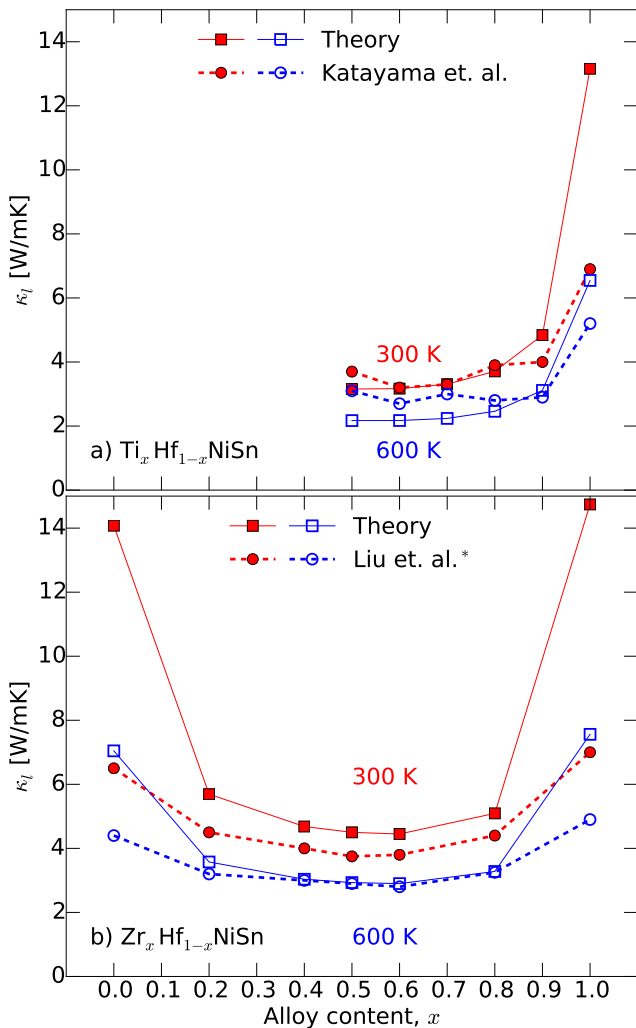


FIG. 4. The lattice thermal conductivity κ_ℓ of the binary HH mixtures $\text{Ti}_x\text{Hf}_{1-x}\text{NiSn}$ (a) and $\text{Zr}_x\text{Hf}_{1-x}\text{NiSn}$ (b) as a function of composition. The present theoretical results are shown as squares connected with solid lines. Circles connected by dotted lines represent experimental results for $\text{Ti}_{1-x}\text{Hf}_x\text{NiSn}$ (a) by Katayama et al.⁶⁶ and $\text{Zr}_{1-x}\text{Hf}_x\text{NiSn}$ (b) by Liu et al.⁵⁶ *The latter experiment was performed on a sample doped with 1.5% Sb on the Sn site. The lines are a guide to the eye. The filled (unfilled) markers correspond to a temperature of 300 (600) K.

disorder scattering. This scatters the more energetic phonon modes most efficiently, just like other localized intrinsic defects, as discussed in the previous section.⁶⁰ However, the added effect of the two mechanisms is much smaller than a naive superposition of the contributions, which gives a significantly less pronounced U shape in experiments than in the modeling without additional localized defects.

We proceed to calculate κ_ℓ for the ternary $\text{Ti}_x\text{Zr}_y\text{Hf}_{1-x-y}\text{NiSn}$ mixtures, where $x, y = 0.1, 0.2, \dots, 1.0$ and $x + y \leq 1$, representing the entire ternary phase diagram. Figure 5 shows contour

plots of the computed κ_ℓ as a function of composition. Panel a) presents the full κ_ℓ including both mass-disorder and three-phonon scattering, whereas panel b) only includes the latter effect. The $\text{Ti}_x\text{Hf}_{1-x}\text{NiSn}$ compositions exhibit the lowest thermal conductivity, with a shallow minimum around $\text{Ti}_{0.5}\text{Hf}_{0.5}\text{NiSn}$. Along the line, between 20% and 80% Ti, κ_ℓ takes values between 3.2 and 4.1 W/mK. Moving from the optimal binary composition to ternary mixtures leads to an increase in κ_ℓ . Note also that the binary mixtures $\text{Ti}_x\text{Zr}_{1-x}\text{NiSn}$ have a significantly higher thermal conductivity than that of corresponding $\text{Zr}_x\text{Hf}_{1-x}\text{NiSn}$ compositions.

Comparing Fig. 5a) with the variation of the mass variance parameter M_{var} (Fig. 1) is a good starting point for discussing the trends in κ_ℓ , because of the central role played by this parameter in mass-disorder scattering; according to eq. (4) a high M_{var} should correspond to a low τ^{md} and thus a small κ_ℓ^{md} . In some ways we can see such a correlation: the highest M_{var} and lowest κ_ℓ are found for binary $\text{Ti}_x\text{Hf}_{1-x}\text{NiSn}$, and the highest κ_ℓ values correspond to the pure $X\text{NiSn}$ compounds, where $M_{\text{var}} = 0$. As mass-disorder scattering efficiently targets the high energetic phonons, the more shallow minima of κ_ℓ along the binary mixture lines than of M_{var} is thus as expected. It is more difficult to explain that M_{var} peaks at about 80% Hf for Ti-Hf mixing, while the minimum κ_ℓ is at 50% Hf. Also remarkable is that M_{var} is similar for Ti-Zr mixing and Zr-Hf mixing, while κ_ℓ is significantly higher for Ti-Zr than for Zr-Hf.

It is tempting to hypothesize that the remaining contribution arises from the anharmonic three-phonon scattering, and we have plotted κ_ℓ^{anh} without mass-disorder scattering, in Fig. 5b) to test this. It is easily concluded that this hypothesis does not hold: In fact, κ_ℓ^{anh} has a *maximum* around $\text{Ti}_{0.5}\text{Hf}_{0.5}\text{NiSn}$, precisely where we should have expected a minimal value in order to move the minimum of the full κ_ℓ to this point. Similarly, κ_ℓ^{anh} is lower along the Ti-Zr line than along Zr-Hf, which is the opposite trend of the total κ_ℓ .

To explain the trends in κ_ℓ^{anh} , we need to consider the full expression for mass-disorder scattering (eq. 4) where the scattering strength is given by a convolution of the PDOS $g_{\mathbf{b}}(\omega)$, phonon-mode amplitude $e_p = |\mathbf{e}(\mathbf{b}|\mathbf{jq})|$, and mass-variance $M_{\text{var}}(\mathbf{b})$ of a given site. Keep in mind that alloying in our case only increases the value of this parameter for the X -site. It is then enlightening to inspect the PDOS of the six compositions shown in Fig. 3. We will later show that the contributions to reducing κ_ℓ originate predominantly from the acoustic modes with frequencies up to about ~ 16 – 18 meV, depending on the composition. Let us first consider the $\text{Ti}_x\text{Hf}_{1-x}\text{NiSn}$ mixture, where M_{var} is relatively large already for a small fraction of Hf (ref. Fig. 1). However, for a small fraction of Hf, the $g_X(\omega)$ (and thus the amplitude e_p) in the relevant frequency range is modest; this can be inferred from interpolating between TiNiSn (Fig. 3a)) and $\text{Ti}_{0.5}\text{Hf}_{0.5}\text{NiSn}$ (Fig. 3f)).

We then compare the trend in the acoustic PDOS

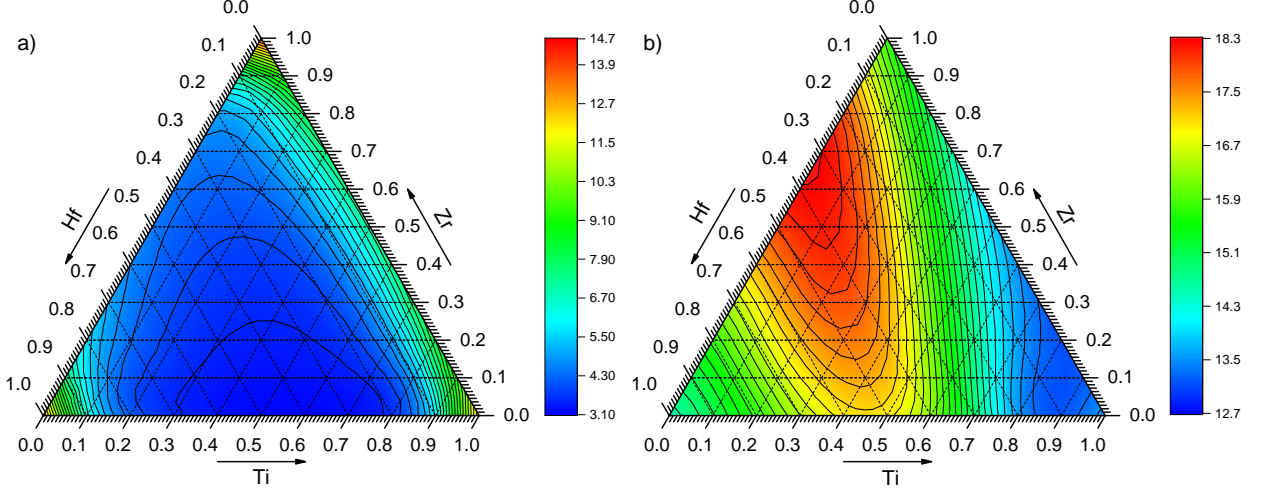


FIG. 5. A ternary map of κ_ℓ for the composition $\text{Ti}_x\text{Zr}_y\text{Hf}_{1-x-y}\text{NiSn}$ at 300 K based on the virtual crystal approximation. The bottom right corner corresponds to TiNiSn , the top to ZrNiSn , and the bottom left to HfNiSn . Panel a) shows the entire κ_ℓ , including anharmonic phonon-phonon scattering and mass-disorder scattering. Panel b) shows κ_ℓ when only the anharmonic phonon-phonon scattering is included through κ_ℓ^{anh} , and mass-disorder scattering is neglected.

when moving from Ti to Hf along the $\text{Ti}_x\text{Hf}_{1-x}\text{NiSn}$ line (Fig. 3a), f), and c)) with the according trend in M_{var} . This shows a trade-off between the maximal M_{var} occurring at $\text{Ti}_{0.8}\text{Hf}_{0.2}\text{NiSn}$ and the maximal $g_X(\omega)$ (and e_p) occurring at HfNiSn . This trade-off results in the minimum position of κ_ℓ being located at $\text{Ti}_{0.5}\text{Hf}_{0.5}\text{NiSn}$. The PDOS of $\text{Zr}_x\text{Hf}_{1-x}\text{NiSn}$, shown in Fig. 3e) for $x=0.5$, has large contributions in the entire acoustic range from the Zr-Hf virtual atom. Thus, along the Zr-Hf line, κ_ℓ is significantly reduced even with a relatively small M_{var} (Fig. 1). Finally, for $\text{Ti}_x\text{Zr}_{1-x}\text{NiSn}$, neither M_{var} (Fig. 1) nor the PDOS of the Ti-Zr site is large (Fig 3d), causing the largest κ_ℓ for this binary composition.

One conclusion to draw from this analysis is that alloying should be performed on sites displaying large PDOS in the acoustic range. One promising possibility for further reduction of κ_ℓ in these compounds is therefore to alloy on the Sn sublattice, in order to avoid using the expensive Hf element to get a low thermal conductivity. The PDOS of TiNiSn in Fig 3c) indicates that the acoustic modes are dominated by vibrations of Sn, so introducing mass-disorder at this site might reduce the thermal conductivity considerably. Isoelectronic substitution of Sn means alloying with Si, Ge, or Pb. It remains to see whether the solubility of these elements is high enough to obtain a significant reduction of κ_ℓ , and whether the other thermoelectric properties are unaffected by such substitutions.

Finally, we remark there are many reports of phase separation in $\text{Ti}_x\text{Zr}_y\text{Hf}_{1-x-y}\text{NiSn}$ samples.⁶⁸⁻⁷⁰ This naturally affects the local compositions and thus the mean lattice thermal conductivity of phase-separated samples. However, the shallow minima in Fig. 5a) indicate the ef-

fect of this would be modest as long as there are stable binary or ternary mixture phases nearby in the phase diagram. More importantly, though, phase separation could reduce the average grain size enhancing grain boundary phonon scattering. In this study, we will not distinguish between different kinds of grain boundaries but rather view phase separation as one of several ways in which a polycrystalline sample could form or stabilize. As discussed in the following, small grain sizes could significantly increase grain-boundary scattering and thus lower the thermal conductivity.

D. The effect of nanostructuring

Mass-disorder does not efficiently scatter the low-frequency part of the acoustic phonon modes, making this range important for heat transport in mixed samples. These long-wavelength modes are particularly sensitive to scattering from boundaries,⁷¹ and nanostructuring hence seems as a promising route to further reduce κ_ℓ in $X\text{NiSn}$ alloys. Scattering from grain boundaries is in this work computed from the simple model defined by eq. (7). This assumes completely diffusive scattering and should give an upper bound of the scattering rate arising from boundary scattering.

Figure 6 shows the lattice thermal conductivity at 300 and 600 K of TiNiSn and $\text{Ti}_{0.5}\text{Hf}_{0.5}\text{NiSn}$ for different average grain sizes when grain boundary scattering is included. κ_ℓ^{GB} typically reaches the bulk (single crystal) value at a grain size of $L = 10 \mu\text{m}$, and is monotonously decreasing as L is reduced. The inset shows the relative reduction of κ_ℓ^{GB} , which is similar for both the mixed

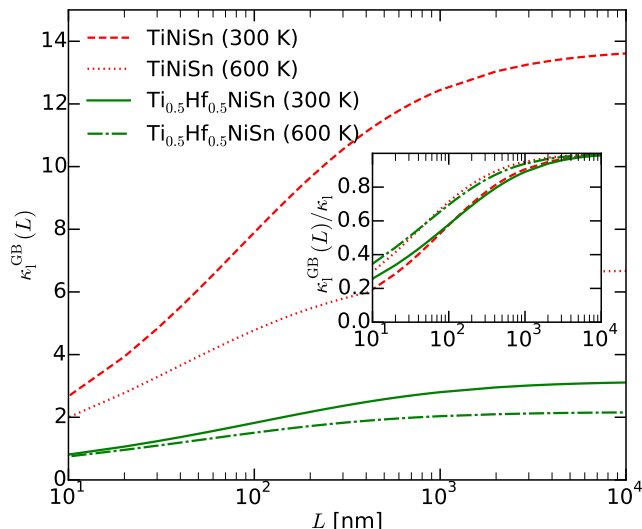


FIG. 6. The total calculated thermal conductivity with grain boundary scattering included κ_ℓ^{GB} , as function of average grain size L for TiNiSn at temperatures 300 K and 600 K (red dashed and dotted) and $\text{Ti}_{0.5}\text{Hf}_{0.5}\text{NiSn}$ at corresponding temperatures (green solid and dashed-dotted). The inset shows the lattice thermal conductivity scaled by the bulk (single crystal) value $\kappa_\ell^{\text{GB}}(L)/\kappa_\ell$ for the four cases.

and pure compounds. A grain size of 100 nm leads to a reduction of the thermal conductivity by more than 40% at $T = 300\text{K}$ and by about a third at $T = 600\text{K}$, compared to the monocrystalline reference. Interestingly, for grain sizes smaller than around 10 nm, κ_ℓ becomes essentially temperature independent, particularly so for the mixed compositions. This can be understood from the grain-boundary scattering model (eq. 7) being explicitly temperature independent. For acoustic phonons in the linear regime, the model is also frequency independent. At higher temperatures, the heat capacity $C_{V,j,q}$ in eq. (2) also varies only slightly with temperature.

Figure 7 displays the cumulative lattice thermal conductivity of TiNiSn and $\text{Ti}_{0.5}\text{Hf}_{0.5}\text{NiSn}$ with and without grain boundary scattering. It shows how, for this optimal composition, mass disorder scattering suppresses contributions from the most energetic phonons. Almost all residual contributions to κ_ℓ arise from frequencies below 10 meV, essentially the linear part of the acoustic phonon spectrum, as seen by comparing to the dispersion in Fig. 2. An interesting feature is that even when including mass-disorder scattering, the contributions to κ_ℓ from frequencies between 3-4 meV are slightly higher in the mixed compositions. This can be linked to the reduced anharmonic phonon scattering rates in the mixed compositions, as seen in Fig. 5.

With information about the scattering efficiency at different phonon frequencies for different scattering mechanisms, it is in principle possible to achieve maximal reduction in κ_ℓ with a tailored combination of mechanisms. As an example, we see in Fig. 7b) that the heat-carrying

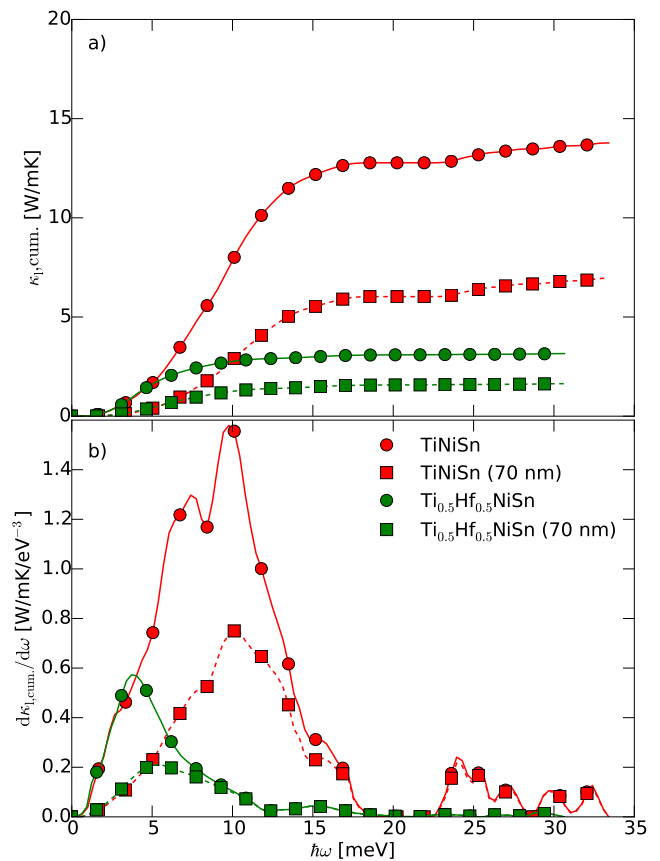


FIG. 7. The cumulative κ_ℓ as a function of phonon frequency given in a) and its derivative in b). Pure TiNiSn with and without grain boundary scattering is shown as red squares and circles, respectively. The composition $\text{Ti}_{0.5}\text{Hf}_{0.5}\text{NiSn}$ with and without grain boundary scattering is shown as green squares and circles.

phonon modes are efficiently scattered between 5–20 meV by mass disorder on the Ti site and between 0–15 meV by grain boundary scattering. When both these mechanisms are active, the remaining contributing phonon modes are centered around 5–10 meV, and any additional engineering of phonon scattering should aim towards this region. One possibility to achieve this is to use even smaller grains sizes to scatter the acoustic region even more strongly. A potential drawback of smaller grains, however, is that this might also significantly reduce the electron conductivity.

IV. CONCLUSION

This study has investigated how various scattering mechanisms lower the thermal conductivity of $X\text{NiSn}$ with isoelectronic sublattice-alloying on the X -site; $X = (\text{Ti}, \text{Zr}, \text{Hf})$. Good agreement was obtained between theory and experiment for mixed compositions, indicating that theory can guide efforts to optimize the ther-

mal conductivity of these materials. By screening the ternary $\text{Ti}_x\text{Zr}_y\text{Hf}_{1-x-y}\text{NiSn}$ phase diagram, we found an optimum at $\text{Ti}_{0.5}\text{Hf}_{0.5}\text{NiSn}$ with a very low thermal conductivity along the $\text{Ti}_x\text{Hf}_{1-x}\text{NiSn}$ line with Ti content between 20 and 80%. Interestingly, the overall trends, for instance, the much lower thermal conductivity along the $\text{Zr}_x\text{Hf}_{1-x}\text{NiSn}$ than the $\text{Ti}_x\text{Zr}_{1-x}\text{NiSn}$ line, can only be understood from a combination of the shifting nature of the phonon modes and the magnitude of the mass variance.

Whereas mass-disorder can be very effective at scattering high energetic phonons and even significantly impact the more energetic acoustic phonons, it is less effective at scattering the acoustic phonons of lowest energy. With a simple model of grain boundary scattering, we find that nanostructuring the sample can further reduce the thermal conductivity. The remaining heat is carried by acoustic phonons that are neither in the low (< 5 meV) nor high (> 10 meV) energy range. Any additional scattering mechanism should therefore target this energy range.

Finally, our analysis demonstrates that the phonon-

mode nature plays a key role in maximizing alloy scattering in these materials. This insight may pave the path to a more general, more deliberate strategy of optimizing the composition of alloyed compounds through phonon-mode engineering. Such engineering could prove crucial by moving high-throughput screening of thermoelectric materials beyond the current emphasis on single unmixed compounds.

ACKNOWLEDGMENTS

The authors gratefully acknowledge a high performance computing allocation from the NOTUR consortium. This work is part of the THELMA project (Project no. 228854) supported by the Research Council of Norway. This project was supported by the German Science Foundation (DFG MA 5487/2-1 and DFG MA5487/1-1). We further thank Matthias Schrader for helpful comments.

-
- ¹ J. Yang and F. R. Stabler, *J. Electron. Mater.* **38**, 1245 (2009).
 - ² L. E. Bell, *Science* **321**, 1457 (2008).
 - ³ J. Carrete, W. Li, N. Mingo, S. Wang, and S. Curtarolo, *Phys. Rev. X* **4**, 011019 (2014).
 - ⁴ R. Gautier, X. Zhang, L. Hu, L. Yu, Y. Lin, T. Sunde, D. Chon, K. Poepfelmeier, and A. Zunger, *Nat. Chem.* **7**, 308 (2015).
 - ⁵ F. Casper, T. Graf, S. Chadov, B. Balke, and C. Felser, *Semiconduct. Sci. Technol.* **27**, 063001 (2012).
 - ⁶ D. Kieven, R. Klenk, S. Naghavi, C. Felser, and T. Gruhn, *Phys. Rev. B* **81**, 075208 (2010).
 - ⁷ J. Shiomi, K. Esfarjani, and G. Chen, *Phys. Rev. B* **84**, 104302 (2011).
 - ⁸ J.-W. G. Bos and R. A. Downie, *J. Phys.: Condens. Matter* **26**, 433201 (2014).
 - ⁹ S. Chen and Z. Ren, *Materials Today* **16**, 387 (2013).
 - ¹⁰ W. G. Zeier, J. Schmitt, G. Hautier, U. Aydemir, Z. M. Gibbs, C. Felser, and G. J. Snyder, *Nat. Rev. Mater.* **1**, 16032 (2016).
 - ¹¹ J. Yang, H. Li, T. Wu, W. Zhang, L. Chen, and J. Yang, *Adv. Funct. Mater.* **18**, 2880 (2008).
 - ¹² T. Zhu, C. Fu, H. Xie, Y. Liu, and X. Zhao, *Adv. Energy Mater.* **5**, 1500588 (2015).
 - ¹³ W. Xie, A. Weidenkaff, X. Tang, Q. Zhang, J. Poon, and T. M. Tritt, *Nanomaterials* **2**, 379 (2012).
 - ¹⁴ G. Joshi, X. Yan, H. Wang, W. Liu, G. Chen, and Z. Ren, *Adv. Energy Mater.* **1**, 643 (2011).
 - ¹⁵ S. J. Poon, D. Wu, S. Zhu, W. Xie, T. M. Tritt, P. Thomas, and R. Venkatasubramanian, *J. Mater. Res.* **26**, 2795 (2011).
 - ¹⁶ Q. Shen, L. Chen, T. Goto, T. Hirai, J. Yang, G. P. Meisner, and C. Uher, *Appl. Phys. Lett.* **79**, 4165 (2001).
 - ¹⁷ C. Uher, J. Yang, S. Hu, D. T. Morelli, and G. P. Meisner, *Phys. Rev. B* **59**, 8615 (1999).
 - ¹⁸ H. Hohl, A. P. Ramirez, C. Goldmann, G. Ernst, B. Wölfing, and E. Bucher, *J. Phys.: Condens. Matter* **11**, 1697 (1999).
 - ¹⁹ T. M. Tritt, S. Bhattacharya, Y. Xia, V. Ponnambalam, S. J. Poon, and N. Thadhani, in *Thermoelectrics, 2001. Proceedings ICT 2001. XX International Conference on* (2001) p. 7.
 - ²⁰ Y. Kawaharada, H. Uneda, H. Muta, K. Kurosaki, and S. Yamanaka, *J. Alloys Compd.* **364**, 59 (2004).
 - ²¹ S. Sakurada and N. Shutoh, *Appl. Phys. Lett.* **86**, 082105 (2005).
 - ²² N. Shutoh and S. Sakurada, *J. Alloys Compd.* **389**, 204 (2005).
 - ²³ Y. Kimura, H. Ueno, and Y. Mishima, *J. Electron. Mater.* **38**, 934 (2009).
 - ²⁴ S. Chen and Z. Ren, *Materials Today* **16**, 387 (2013).
 - ²⁵ R. A. Downie, D. A. MacLaren, and J.-W. G. Bos, *J. Mater. Chem. A* **2**, 6107 (2014).
 - ²⁶ K. Gałazka, S. Populoh, L. Sagarna, L. Karvonen, W. Xie, A. Beni, P. Schmutz, J. Hulliger, and A. Weidenkaff, *Phys. Status Solidi A* **211**, 1259 (2014).
 - ²⁷ S. Bhattacharya, T. M. Tritt, Y. Xia, V. Ponnambalam, S. J. Poon, and N. Thadhani, *Appl. Phys. Lett.* **81**, 43 (2002).
 - ²⁸ S. Bhattacharya, M. J. Skove, M. Russell, T. M. Tritt, Y. Xia, V. Ponnambalam, S. J. Poon, and N. Thadhani, *Phys. Rev. B* **77**, 184203 (2008).
 - ²⁹ C. Yu, T.-J. Zhu, R.-Z. Shi, Y. Zhang, X.-B. Zhao, and J. He, *Acta Mater.* **57**, 2757 (2009).
 - ³⁰ C. Yu, T.-J. Zhu, K. Xiao, J.-J. Shen, S.-H. Yang, and X.-B. Zhao, *J. Electron. Mater.* **39**, 2008 (2009).
 - ³¹ A. Bhardwaj, D. Misra, J. Pulikkotil, S. Auluck, A. Dhar, and R. Budhani, *Appl. Phys. Lett.* **101** (2012).
 - ³² H.-H. Xie, C. Yu, T.-J. Zhu, C.-G. Fu, G. Jeffrey Snyder, and X.-B. Zhao, *Appl. Phys. Lett.* **100** (2012).

- ³³ J. R. Sootsman, R. J. Pcionek, H. Kong, C. Uher, and M. G. Kanatzidis, *Chem. Mater.* **18**, 4993 (2006).
- ³⁴ A. J. Minnich, M. S. Dresselhaus, Z. F. Ren, and G. Chen, *Energy Environ. Sci.* **2**, 466 (2009).
- ³⁵ Z.-G. Chen, G. Han, L. Yang, L. Cheng, and J. Zou, *Progress in Natural Science: Materials International* **22**, 535 (2012).
- ³⁶ A. Togo, L. Chaput, and I. Tanaka, *Phys. Rev. B* **91**, 094306 (2015).
- ³⁷ G. P. Srivastava, *The Physics of Phonons* (CRC Press, 1990).
- ³⁸ B. Abeles, *Phys. Rev.* **131**, 1906 (1963).
- ³⁹ S.-i. Tamura, *Phys. Rev. B* **30**, 849 (1984).
- ⁴⁰ Z. Tian, J. Garg, K. Esfarjani, T. Shiga, J. Shiomi, and G. Chen, *Phys. Rev. B* **85**, 184303 (2012).
- ⁴¹ J. Garg, N. Bonini, B. Kozinsky, and N. Marzari, *Phys. Rev. Lett.* **106**, 045901 (2011).
- ⁴² W. Li, L. Lindsay, D. A. Broido, D. A. Stewart, and N. Mingo, *Phys. Rev. B* **86**, 174307 (2012).
- ⁴³ A. Katre, A. Togo, I. Tanaka, and G. K. H. Madsen, *J. Appl. Phys.* **117**, 045102 (2015).
- ⁴⁴ Z. Tian, K. Esfarjani, and G. Chen, *Phys. Rev. B* **86**, 235304 (2012).
- ⁴⁵ X. Li and R. Yang, *Phys. Rev. B* **86**, 054305 (2012).
- ⁴⁶ K. Kirievsky, M. Shlimovich, D. Fuks, and Y. Gelbstein, *Phys. Chem. Chem. Phys.* **16**, 20023 (2014).
- ⁴⁷ L. Bjerg, B. B. Iversen, and G. K. H. Madsen, *Phys. Rev. B* **89**, 024304 (2014).
- ⁴⁸ J. M. Ziman, *Electrons and Phonons: The Theory of Transport Phenomena in Solids* (Oxford Classic Texts in the Physical Sciences, 1960).
- ⁴⁹ G. Kresse and D. Joubert, *Phys. Rev. B* **59**, 1758 (1999).
- ⁵⁰ J. P. Perdew, K. Burke, and M. Ernzerhof, *Phys. Rev. Lett.* **77**, 3865 (1996).
- ⁵¹ A. Togo and I. Tanaka, *Scr. Mater.* **108**, 1 (2015).
- ⁵² P. Giannozzi, S. de Gironcoli, P. Pavone, and S. Baroni, *Phys. Rev. B* **43**, 7231 (1991).
- ⁵³ X. Gonze and C. Lee, *Phys. Rev. B* **55**, 10355 (1997).
- ⁵⁴ L. Andrea, G. Hug, and L. Chaput, *J. Phys.: Condens. Matter* **27**, 425401 (2015).
- ⁵⁵ H. Muta, T. Kanemitsu, K. Kurosaki, and S. Yamanaka, *Mater. Trans.* **47**, 1453 (2006).
- ⁵⁶ Y. Liu, H. Xie, C. Fu, G. J. Snyder, X. Zhao, and T. Zhu, *J. Mater. Chem. A* **3**, 22716 (2015).
- ⁵⁷ M. Wambach, R. Stern, S. Bhattacharya, P. Ziolkowski, E. Müller, G. K. Madsen, and A. Ludwig, *Adv. Electron. Mater.* **2**, 1500208 (2016).
- ⁵⁸ H. Xie, H. Wang, C. Fu, Y. Liu, G. Snyder, X. Zhao, and T. Zhu, *Sci. Rep.* **4**, 6888 (2014).
- ⁵⁹ R. Stern, B. Dongre, and G. K. H. Madsen, *Nanotechnology* **27**, 334002 (2016).
- ⁶⁰ A. Katre, J. Carrete, and N. Mingo, *J. Mater. Chem. A* **4**, 15940 (2016).
- ⁶¹ J. E. Douglas, P. A. Chater, C. M. Brown, T. M. Pollock, and R. Seshadri, *J. Appl. Phys.* **116**, 163514 (2014).
- ⁶² H. Hazama, M. Matsubara, R. Asahi, and T. Takeuchi, *J. Appl. Phys.* **110**, 063710 (2011).
- ⁶³ J. E. Douglas, C. S. Birkel, N. Verma, V. M. Miller, M.-S. Miao, G. D. Stucky, T. M. Pollock, and R. Seshadri, *J. Appl. Phys.* **115**, 043720 (2014).
- ⁶⁴ D. Do, S. Mahanti, and J. Pulikkoti, *J. Phys.: Condens. Matter* **26**, 275501 (2014).
- ⁶⁵ A. Page, C. Uher, P. F. Poudeu, and A. Van der Ven, *Phys. Rev. B* **92**, 174102 (2015).
- ⁶⁶ T. Katayama, S. W. Kim, Y. Kimura, and Y. Mishima, *J. Electron. Mater.* **32**, 1160 (2003).
- ⁶⁷ T. Feng and X. Ruan, *Phys. Rev. B* **93**, 045202 (2016).
- ⁶⁸ H. Geng and H. Zhang, *J. Appl. Phys.* **116**, 033708 (2014).
- ⁶⁹ A. Page, A. Van der Ven, P. F. P. Poudeu, and C. Uher, *J. Mater. Chem. A* **4**, 13949 (2016).
- ⁷⁰ M. Gürth, G. Rogl, V. Romaka, A. Grytsiv, E. Bauer, and P. Rogl, *Acta Materialia* **104**, 210 (2016).
- ⁷¹ H. Goldsmid and A. Penn, *Phys. Lett. A* **27**, 523 (1968).